2012

Barriers to front propagation in ordered and disordered vortex flows

Dylan Bargteil
Bucknell University, dzb002@bucknell.edu

Tom Solomon
Bucknell University, tsolomon@bucknell.edu

Barriers to front propagation in ordered and disordered vortex flows

Dylan Bargteil and Tom Solomon

Citation: Chaos **22**, 037103 (2012); doi: 10.1063/1.4746764
View online: http://dx.doi.org/10.1063/1.4746764
View Table of Contents: http://chaos.aip.org/resource/1/CHAOEH/v22/i3
Published by the American Institute of Physics.

Barriers to front propagation in ordered and disordered vortex flows

Dylan Bargteil[a] and Tom Solomon[b]
Department of Physics and Astronomy, Bucknell University, Lewisburg, Pennsylvania 17837, USA

(Received 14 April 2012; accepted 31 July 2012; published online 28 September 2012)

We present experiments on reactive front propagation in a two-dimensional (2D) vortex chain flow (both time-independent and time-periodic) and a 2D spatially disordered (time-independent) vortex-dominated flow. The flows are generated using magnetohydrodynamic forcing techniques, and the fronts are produced using the excitable, ferroin-catalyzed Belousov-Zhabotinsky chemical reaction. In both of these flows, front propagation is dominated by the presence of *burning invariant manifolds* (BIMs) that act as barriers, similar to invariant manifolds that dominate the transport of passive impurities. Convergence of the fronts onto these BIMs is shown experimentally for all of the flows studied. The BIMs are also shown to collapse onto the invariant manifolds for passive transport in the limit of large flow velocities. For the disordered flow, the measured BIMs are compared to those predicted using a measured velocity field and a three-dimensional set of ordinary differential equations that describe the dynamics of front propagation in advection-reaction-diffusion systems. © *2012 American Institute of Physics*. [http://dx.doi.org/10.1063/1.4746764]

The dynamics of a wide range of reacting systems can be characterized by the propagation of fronts that separate distinct phases in the reacting system. Such fronts can be defined for systems such as wildfires, plasmas,[1] plankton blooms,[2] epidemics,[3] phase transitions in matter,[4] and chemical reactions.[5,6] The behavior of reaction fronts has been well-studied in the *reaction-diffusion* (RD) limit, i.e., in a stagnant system in which molecular diffusion is the dominant mixing mechanism. In many real systems, however, the propagation of fronts is strongly influenced by the presence of fluid flows. The behavior of these more general *advection-reaction-diffusion* (ARD) systems has been studied extensively for turbulent flows, especially for engineering applications involving turbulent combustion. The propagation of fronts in laminar flows or in flows with large coherent structures, however, is still poorly understood. This is a problem with significant applications, e.g., in microfluidic chemical reactions,[7] cellular or embryonic scale biological systems,[8,9] and population dynamics in oceanic flows with large-scale coherent vortices.[10] In this paper, we present experiments on front propagation in a simple, laminar flow composed of a chain of alternating vortices and in a spatially disordered, vortex-dominated flow. We show that front propagation is dominated by local barriers in the flow called *burning invariant manifolds*[11] (BIMs) which could form the basis for a general theory of front propagation in ARD systems. These BIMs are generalizations of invariant manifolds that act as barriers to transport of passive impurities. The BIMs are shown to be directional—they block fronts propagating in one direction but allow fronts propagating the opposite way to pass through. We demonstrate experimentally how BIMs can be measured in both time-independent and time-periodic fluid flows, and we show that the BIMs collapse onto the invariant manifolds for passive transport in the limit of large flow velocities.

I. INTRODUCTION

It is well known[12,13] that mixing of passive impurities in laminar fluid flows can be chaotic with nearby tracers separating exponentially in time, resulting in significant enhancements in mixing. Mixing and transport in time-independent and time-periodic flows can be characterized by invariant manifolds[14,15] which act as transport barriers, along with their intersections (or "lobes") which have been used to analyze long-range transport.[15–17] Although originally developed to describe passive transport in simple time-independent and time-periodic flows, the concept of the invariant manifold has been extended to a wide range of flows, based on an approach that identifies *Lagrangian coherent structures* (LCS) in the flows, manifold-like structures which act as temporary barriers to transport.[18] LCS approaches have been used successfully to describe transport in several systems of significant practical importance, including pollution mitigation in Monterey Bay[19] and near the coast off Florida[20] and predictions of the path of oil flowing from oil spills in the Gulf of Mexico.[21,22]

In a recent article,[11] a new approach based on invariant manifolds was proposed to describe the behavior of *reaction fronts* propagating in a fluid flow. Here, we present experiments that test this approach for analyzing front propagation in predominately two-dimensional (2D) laminar flows. Similar to the role played by invariant manifolds as barriers for passive transport, structures called burning invariant manifolds (BIMs) act as one-way barriers for front propagation in ARD systems.[11] We test these ideas experimentally in ordered flows consisting of a chain of alternating vortices (both time-independent and time-periodic) and in a spatially disordered, vortex-dominated flow. We use the excitable, ferroin-catalyzed Belousov-Zhabotinsky (BZ) chemical reaction,[6,23] which produces pulse-like reaction fronts that can be

[a]Current address: Department of Physics, New York University, New York, New York, 10003, USA.
[b]Electronic mail: tsolomon@bucknell.edu.

triggered in a controlled manner. We experimentally identify BIMs for chemical fronts propagating in these flows and analyze these BIMs based on a three-dimensional (3D) mathematical formalism.

In Sec. II, we present background about invariant manifolds for passive transport, previous experiments on front propagation in vortex flows, and the theory of burning invariant manifolds. The experimental techniques used for investigating BIMs in both the vortex chain and disordered vortex flow are explained in Sec. III. Experimental results illustrating BIMs in the vortex chain flows are presented in Sec. IV. The results for the spatially disordered flows are shown in Sec. V. Section VI presents a discussion of these results, along with continuing experiments.

II. BACKGROUND

A. Passive mixing and invariant manifolds

The vortex chain flow (Fig. 1) has become a paradigm in studies of passive mixing. If the flow is time-independent, tracers follow closed trajectories, never leaving whichever vortex they are initially in. If molecular diffusion is included, long-range transport can occur via advection of tracers around a vortex and diffusion across the boundary between one vortex and the next. The result[24,25] is long-range transport where the variance $\langle x^2 \rangle$ grows linearly in time: $\langle x^2 \rangle = 2D^* t$, where D^* is an enhanced diffusion coefficient which is typically a couple of orders of magnitude larger than the molecular diffusion coefficient. If the vortex chain oscillates periodically in a lateral direction, tracers can be advected between vortices, following chaotic trajectories with nearby tracers separating exponentially in time.[26] Transport in this case is usually also diffusive in nature, although there are very narrow frequency ranges where transport is superdiffusive (with $\langle x^2 \rangle \sim t^\gamma$ with $1 < \gamma < 2$) for significant transient times.[27]

When analyzing passive mixing theoretically, one typically follows the motion of an infinitesimal fluid element or a passive impurity in the flow. If the flow is time-independent, then the x- and y-coordinates of the impurity fully specify the velocity field at that point, which allows for prediction of the time-evolution of the tracer's location; consequently, a 2D phase space describes the kinematics of the impurity. If the flow is time-periodic, then there is a third dimension associated with the phase of the oscillation. This third time-dimension is usually accounted for with the use of Poincaré sections which plot the tracer's location once every period.

For the vortex chain flow of Fig. 1, passive mixing can be characterized by integration of the x- and y-velocity field[26]

$$\begin{aligned} dx/dt &= u_x(x,y,t) = \sin(\pi[x + b\sin(\omega t)])\cos(\pi y), \\ dy/dt &= u_y(x,y,t) = -\cos(\pi[x + b\sin(\omega t)])\sin(\pi y). \end{aligned} \quad (1)$$

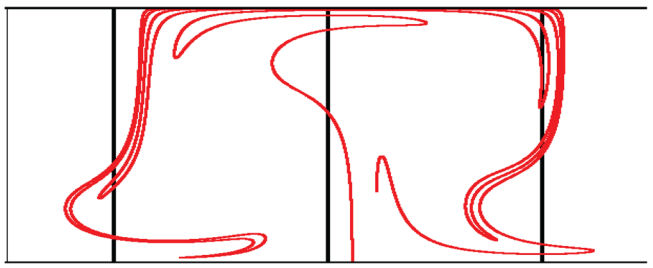

FIG. 2. Invariant manifolds for passive transport in vortex chain flow. The vertical (black) lines show the boundaries between adjacent vortices; these lines are also the invariant manifolds for passive transport for a time-independent (stationary) flow. The other (red) curve is an invariant manifold for a time-periodic flow where the vortices oscillate laterally.

In these equations, x, y, and the oscillation amplitude b are non-dimensionalized by the vortex width D, and the velocity is non-dimensionalized by maximum flow speed U. This is a simplified model that assumes a purely 2D flow with free-slip boundary conditions. This model has been used very successfully during the past 20 years to analyze both passive transport[16,17,26] and front propagation[11,28–32] in experiments with vortex chain flows, even though the experiments have no-slip boundary conditions and typically have a weak, secondary, 3D flow due to Ekman pumping.[33]

Transport in the vortex chain can be understood by considering fixed points in the flow and invariant manifolds attached to those fixed points. Figure 2 shows an example of invariant manifolds for passive transport for both the time-independent and time-periodic vortex chain flows. The vertical (black) lines denote the boundaries between adjacent vortices in the flow, which also happen to be the invariant manifolds for passive transport for a time-independent flow. The Eulerian (hyperbolic) fixed points are at the ends of these manifolds. The folded curve (red) corresponds to a periodic (oscillatory) flow; this is the unstable manifold of the bottom, middle fixed point for that flow. The manifolds are defined as the set of points that would advect to the unstable fixed point under time reversal. To numerically compute the manifolds, we initially locate a large number of tracers very close to the bottom, middle fixed point. The positions of these tracers are integrated numerically for several periods of oscillation of the vortex chain, during which the tracers map out the manifold.[34] The complicated folding structure seen here is typical of manifolds for chaotic mixing.

An invariant manifold acts as an impenetrable barrier across which no tracers can pass in either direction in the absence of molecular diffusion. For a time-independent flow, the manifolds effectively isolate the individual vortices in the flow; no tracers can cross from one vortex to the next without diffusion. The manifolds are impenetrable barriers in the time dependent case as well. This does not, however, prevent long-range transport of impurities across the system,

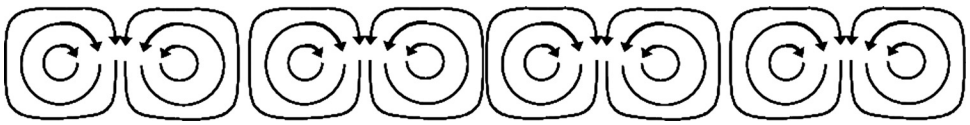

FIG. 1. Chain of alternating vortices.

since the manifold is stretched and folded repeatedly, resulting in a manifold structure that spans many vortices in the flow. In fact, were the simulation continued indefinitely, the manifold would stretch and fold into an infinite-hierarchical structure that covers all of the vortices in the system. Tracers in the flow can never cross the manifold, but they can follow the manifold as it stretches and folds through the vortex chain.

B. Front propagation

The speed at which a front propagates through a system with no advection (i.e., in the RD regime) is well-described by the Fisher-Kolmogorov-Petrovskii-Piskunov (FKPP) theory: $V_0 = 2\sqrt{D_0/\tau}$, where D_0 is the molecular diffusion coefficient of the reacting components and τ is reaction time scale.[35,36] When a vortex chain flow is added (Fig. 1), it is reasonable to propose that a reaction front propagating in this ARD system will propagate at a speed that is still described by the FKPP prediction, but with the molecular diffusivity D_0 replaced with the enhanced diffusivity D^*. Previous studies of reaction fronts in the oscillatory vortex chain, however, found a very different result.[30–32] Reaction fronts in this case often mode-lock to external forcing, propagating an integer number of vortex pairs in an integer number of drive periods. These time-periodic flows exhibit enhanced diffusion coefficients orders of magnitude larger than for the time-independent vortex chain, yet the mode-locking causes some fronts to move *slower* than in the unforced case. The mode-locking results imply that an extension of FKPP theory is not sufficiently general for ARD systems.

Subsequent experiments[37,38] have indicated that the addition of a uniform "wind" to the vortex flow results in fronts that are often pinned to a vortex for a wide range of imposed wind speeds, propagating neither forward against the wind nor being blown backward. Based on this pinning result, the mode-locking observed for the time-periodic flow can qualitatively be explained as a ratcheting mechanism due to periodic pinning from what can be thought of as an oscillatory imposed wind. This heuristic argument, however, does not provide a complete theory to explain the origins of the mode-locking nor does it give sufficient insight into front propagation in a wide range of laminar flows. Ultimately, a new approach is needed.

C. Burning invariant manifolds

A recent paper[11] introduced a general, geometric theory of front propagation in laminar ARD systems motivated by the theory of invariant manifolds in advection discussed in Sec. II A. That theory, which we describe in this section, forms the basis for the analysis in this paper.

Whereas the passive transport problem requires a 2D system of ordinary differential equations (ODEs), the analysis of the motion of a front requires an additional variable. In addition to the x- and y-coordinates of a small section of the front, it is also necessary to specify the angle θ that the front makes with respect to the horizontal. This results in an expanded, 3D set of differential equations to describe front dynamics

$$\dot{x} = u_x + v_0 \sin\theta, \quad \dot{y} = u_y - v_0 \cos\theta, \tag{2a}$$

$$\dot{\theta} = -2u_{x,x} \sin\theta\cos\theta - u_{x,y}\sin^2\theta + u_{y,x}\cos^2\theta, \tag{2b}$$

where (x, y, θ) is the position and orientation of a front element, $\mathbf{u}$ is the fluid flow velocity vector field, and v_0 is RD burn speed (V_0) non-dimensionalized by the maximum flow speed U. The first term in each of Eqs. (2a) represents advection of the front with the 2D flow, and the second term in each of Eqs. (2a) represents the reactive burning of the front relative to the flow, in a direction perpendicular to the front. Equation (2b) quantifies the rotation of a front due to the flow.[11] This system of equations assumes an incompressible flow; furthermore, we assume a constant front propagation speed for a given reaction and do not model local variations in v_0 due to front curvature. The reaction is assumed not to feed back on the velocity field in this model. It is also interesting to note that the model presented here in Eqs. (2a) and (2b) is equivalent to the set of equations of motion for self-propelled elongated particles in flows with chaotic advection.[39,40]

In the same way that the 2D ODEs for passive transport have stationary solutions (fixed points) with attached stable and unstable manifolds, this expanded 3D model also has fixed points with attached manifolds, which we call *burning fixed points* and BIMs, respectively. The BIMs are infinite, 1D curves in a 3D phase space. To make physical sense of them, we project them down from the 3D phase space onto the 2D physical, xy-space.

We can use the non-dimensional RD front velocity $v_0 = V_0/U$ to identify several distinct regimes. The FKPP regime is recovered in the limit in which the advection in an ARD system vanishes, i.e., $v_0 \to \infty$. In this regime, there are no fixed points or manifolds. The passive mixing regime is recovered in the opposite limit, when $v_0 \to 0$, i.e., advection with the flow overwhelms the reaction-diffusion dynamics. In this regime, the burning fixed points are the same as the Eulerian fixed points, and the BIMs are the same as the passive invariant manifolds.

In the intermediate regime (finite v_0), the hyperbolic fixed points for passive transport split into two burning fixed points. A reaction triggered at an Eulerian fixed point in the flow is not a stationary solution of the 3D dynamics. The reaction will burn outward from the advective fixed point until it approaches the burning fixed points, which are the points where the local advection is equal in magnitude to v_0 but opposed to the burning direction. In analogy with the invariant manifolds of the passive case ($v_0 \to 0$), the BIMs extend from the burning fixed points.

Similar to invariant manifolds for passive transport, BIMs act as barriers to front propagation in ARD systems. However, BIMs act as *oriented* (one-way) barriers to front propagation, blocking reactions impinging in one direction but allowing reactions propagating in the opposite direction to pass.

III. EXPERIMENTAL TECHNIQUES

For our investigation, we utilize the excitable, ferroin-catalyzed BZ reaction[41]—a solution composed of 0.22 M

sulfuric acid, 0.36 M sodium bromate, 0.12 M Malonic acid, and 0.12 M sodium bromide is mixed under a vent hood until clear, and then 0.025 M ferroin indicator is added turning the solution a deep orange color. (More ferroin is added during the course of the experiments over several hours as the color fades.) The entire solution is poured into the apparatus. A reaction front is triggered by the insertion of a silver wire in the flow, which oxidizes the indicator in the vicinity of the wire, changing the color of the fluid in that region from orange to blue. This region then oxidizes the fluid nearby, producing a front that propagates outward from the trigger point. In all experiments, the front propagation speed V_0 in the absence of a flow is 0.007 cm/s. The reaction is excitable: it relaxes back to its original orange color after about a minute and can be re-triggered. To subdue undesired, spontaneous self-triggering in the larger disordered flow system, a sodium bromide inhibitor is added near the side-walls of the apparatus where spontaneous self-triggering is the most problematic. The BZ reaction is electrolytic in both its unreacted and reacted phases.

Both the vortex chain and the spatially disordered flow are generated using magnetohydrodynamic forcing techniques[17,41,42] (Fig. 3). We place a plexiglass container with a thin (2 mm) layer of the chemicals comprising the BZ reaction above an arrangement of permanent magnets and then pass a current horizontally through the fluid. The current interacts with the magnetic field to produce a Lorentz force that drives a horizontal flow in the fluid layer.

The vortex chain flow uses a strip of 1.9 cm diameter Nd-Fe-Bo magnets arranged in a line with alternating polarity mounted on a translation stage. The container holding the fluid has a flow channel measuring 1.9 cm × 27 cm (bounded by thin plastic strips) placed directly over the strip of magnets. Passing DC current (using a constant current power supply) lengthwise through the channel generates a steady flow of counter-rotating vortices, each with width $D = 1.9$ cm and unity aspect ratio, as in Fig. 1. By using the translation stage to laterally oscillate the magnets under the flow channel, we can oscillate the vortices.

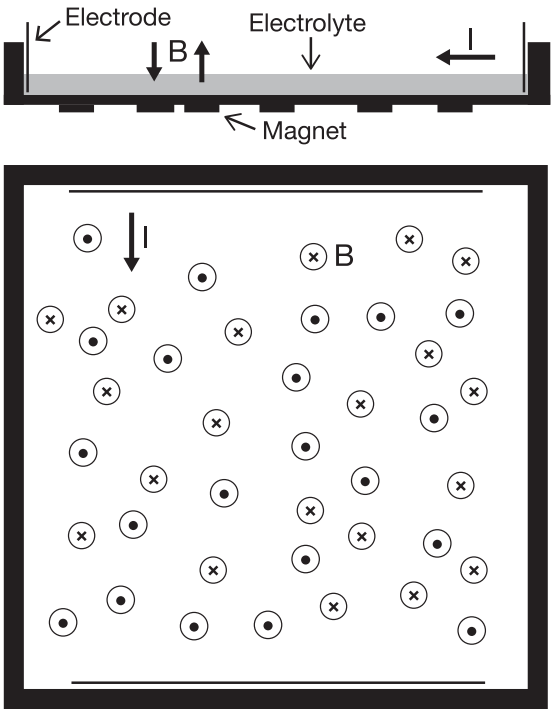

FIG. 3. Schematics of the disordered vortex flow apparatus. Top: Side view of apparatus. A spatially disordered array of magnets is placed under a container of electrolytic solution. A DC electrical current is passed through the solution using two electrodes. Bottom: Top view of the apparatus. Magnetic field is shown entering or exiting the plane of the image.

The disordered vortex array uses an arrangement of 558 Nd-Fe-Bo magnets with 0.6 cm diameter placed under a 28 cm square container (Fig. 3). The magnets are arranged with no ordering in their spatial distribution or polarity. Passing DC current through the fluid generates a disordered, vortex-dominated flow that is time-independent.

While the flow field for the oscillating vortex chain can be modeled easily (Eq. (1)), the flow field for the disordered vortex array is unknown and needs to be measured experimentally. In order to measure the velocity field of the disordered flow, we introduce the BZ reagents into the cell without the ferroin catalyst or powdered chemical reactants. This mixture—which is still electrolytic—has a kinematic viscosity that is nearly identical to the BZ reaction that we use to make other measurements; consequently, passing the same current through this mixture should result in approximately the same flow that occurs with the BZ reaction. We then place 500 μm black tracer particles in the fluid over a white background, illuminate them using an LCD projector, and image them roughly three times per second using a CCD camera with a 50 ms exposure time. We then use these sequences of images to locate the particles in each frame and track their motion through time.

Velocity data for the disordered flow are calculated by fitting parametric parabolas to the x- and y-coordinates over short intervals of time. Derivatives of these parametric fits are then used to calculate the x- and y-components of the velocity. Due to the difficulty of sampling the entire flow with particles, as well as the irregularity of the points at which we calculate the velocities of tracer particles, we interpolate our sparse velocity data onto a uniform grid using Delaunay triangles and cubic splines.

The magnetohydrodynamic forcing is not the only thing driving fluid motion in these experiments. The propagating chemical reaction itself produces small density gradients that can drive buoyancy-forced convection; furthermore, since the fluid has a free surface, temperature gradients from the reaction also induce Marangoni convection.[43–47] The velocities associated with these reaction-driven flows are typically around 50 times slower than the flows driven magnetohydrodynamically in these experiments; consequently, we do not consider the effects of these reaction-driven flows on the dynamics of the propagating front nor as part of our model flow 1. For systems with weaker or no externally imposed flows, however, it would be important to consider the effects of reaction-driven flows in the system.

IV. RESULTS: VORTEX CHAIN FLOW

The evolution of a single reaction front triggered at a fixed point in a time-independent flow can be used to identify

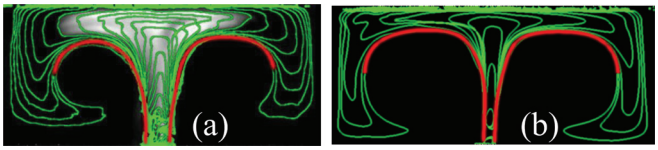

FIG. 4. Sequence of fronts for time-independent flows, along with the experimentally extracted BIMs (in red). (a) Maximum flow speed $U = 0.045$ cm/s, $v_0 = 0.16$. (b) $U = 0.090$ cm/s, $v_0 = 0.078$.

BIMs in the vicinity. Figure 4 shows the evolution of reactions triggered in this manner for two different values of v_0. If a reaction front is triggered at the Eulerian fixed point between two BIMs, the front propagates in a channel bounded by these two BIMs, shown in red in both panels of Fig. 4. As expected, the BIMs for a flow with large v_0 (Fig. 4(a)) are farther from the passive manifold, and the BIMs are closer to the passive manifold if v_0 is smaller (Fig. 4(b)).

The flow is not perfectly two-dimensional in these vortex flows; rather, there is a small, three-dimensional secondary flow—Ekman pumping[33]—that can cause some slight penetration of reaction fronts through BIMs. Nevertheless, the fronts can be shown to converge quite well onto the BIMs. Figure 5 shows the approach of a front to the topmost portion of the right BIM in Fig. 4(a), along with a line whose slope denotes the speed V_0 for a reaction front in the absence of a flow. The front slows down asymptotically to a speed which is an order of magnitude smaller than V_0, indicating good convergence.

The BIMs are more complicated for a vortex chain with periodic time dependence (Figs. 6 and 7). First, since the flow is periodic, the BIMs undulate periodically in time, so a sequence of fronts from a single trigger event is not sufficient to visualize the BIMs. Instead, the BIMs are determined by doing a series of experiments, each in which a front is triggered at the Eulerian fixed point (which oscillates back and forth) at different phases of the oscillation. For each experiment, the front evolves in time, and we take a snapshot of the front at a phase of 0, i.e., when the lateral oscillation crosses the mid-point in the positive direction.[48] The fronts—from all of these experiments—imaged at these phases are displayed in Figs. 6 and 7. As with the simpler time-independent case, these images reveal the BIMs as bounding curves that form a channel through which the front evolves. The images are not perfect because the BIMs are close together near the Eulerian fixed point; consequently, the initial trigger occasionally overlaps one of the BIMs, and part of the evolving front in those cases starts outside the channel formed by the BIMs.

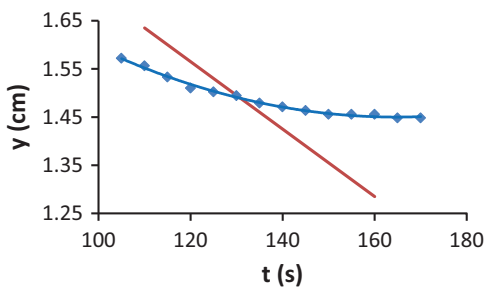

FIG. 5. Convergence of reaction front to a BIM. The blue symbols show the bottom-most edge of the downward-propagating reaction above the highest point of the right BIM in Fig. 4(a). The straight line (red) shows the speed V_0 at which a front would propagate in the absence of any flow. The ARD front slows to a speed an order of magnitude smaller than V_0.

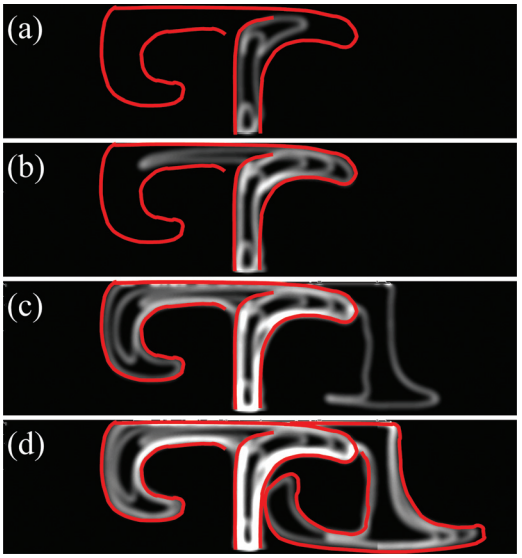

FIG. 6. Sequence of fronts for time-periodic flow with $U = 0.090$ cm/s ($v_0 = 0.078$), oscillating with frequency $\Omega = 0.16$ rad/s and (non-dimensional) amplitude $b = 0.15$. Time after trigger for fronts (in multiples of the oscillation period T) are (a) 0.3, 0.9, and 1.0; (b) 1.1 and 1.4; (c) 1.5 and 1.8; and (d) 1.9 and 2.1. (Each image includes the previous fronts.) Edge enhancements of the fronts are shown, in order to make it possible to see multiple fronts in the same image. The red curves in (a)-(c) show the experimentally extracted BIMs for the first two periods of oscillation of the vortex chain, and the additional red curve in (d) shows a continuation of the right-part of the BIMs after an additional oscillation period.

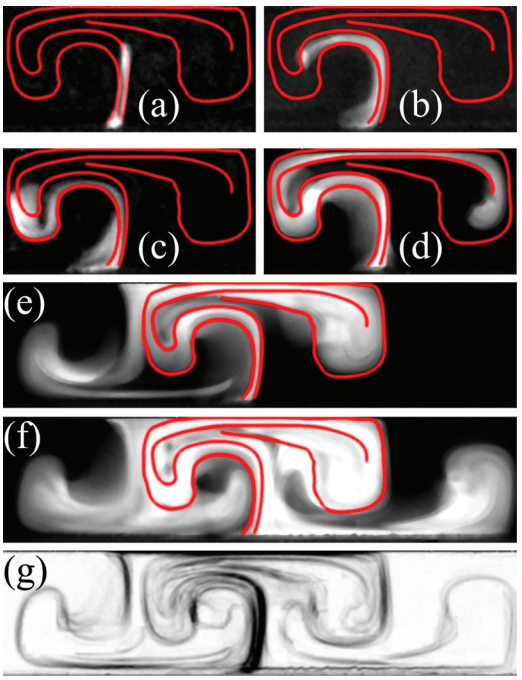

FIG. 7. Sequence of images showing BIMs for a time-periodic flow with $U = 0.090$ cm/s ($v_0 = 0.0078$), $\Omega = 0.16$ rad/s, and $b = 0.30$. Time after trigger for fronts (in multiples of the oscillation period T) is (a) 0.42, (b) 0.55, (c) 0.87, (d) 1.10, (e) 1.60, and (f) 2.10. The red curves show the BIMs surrounding the bottom center Eulerian fixed point. (g) shows a superposition of gradient-enhanced images; ridges in this image help in determination of the BIM structure.

The BIMs for the time-periodic case are determined by a combination of two approaches. Figure 7(g) shows a superposition of gradient enhanced images—each taken from the same phase of oscillation—which has ridges (maxima) in regions where the moving fronts tend to be blocked. The ridges in the superposition image give a first approximation of the structure of the BIMs. This gradient method is less effective for the time-periodic case than for the time-independent case, since only the images from the same phase of oscillation can be used, significantly limiting the amount of data that can be added to the superposition image. The second approach uses sequences of fronts, shown in Figs. 6 and 7. Since the fronts in these images are triggered predominately between a pair of BIMs, they approach and converge on the BIMs, which form a channel through which the front evolves. So, as in the time-independent case (Fig. 4), the BIMs are revealed as the bounding curves in these images.

The red curves in Figs. 6 and 7 show our best estimate of the BIMs for the middle, bottom fixed point. (There are BIMs associated with all of the burning fixed points in the flow.) These curves show only part of each BIM; with each oscillation period, the reaction front is extended, revealing more of the BIM, as shown in Fig. 6. The right-most part of the BIMs in Fig. 6(c) maps one period later to the additional portion of the BIMs shown in Fig. 6(d). This behavior is similar to that of the invariant manifolds for passive transport (Fig. 2). In the same manner that passive impurities in a time-periodic flow can be transported many vortices by following the periodically undulating manifold, a reaction front can propagate an arbitrarily large number of vortices by following the periodically undulating BIM.

There are two significant differences between manifolds for passive transport and BIMs for propagating reactions. First, even though a passive manifold is stretched and folded an arbitrarily large number of times, there is no segment of a passive manifold that ever spans the channel of the vortex chain, i.e., from the top to the bottom in any of the images of the vortex chain. A BIM, however, can have segments that span from one boundary to the opposite, e.g., the left BIM in Fig. 7. A spanning BIM does not necessarily cut off long-range front propagation for time-periodic flows since the BIMs undulate periodically, with the front following the undulating BIM.

A second significant difference is the fact that BIMs are directional. Figure 8 shows two different experiments with fronts propagating in opposite directions and impinging on the same set of BIMs. In each case, the front passes through the first BIM and is then blocked by the second BIM. This is in contrast to manifolds for passive transport that block mixing in either direction.

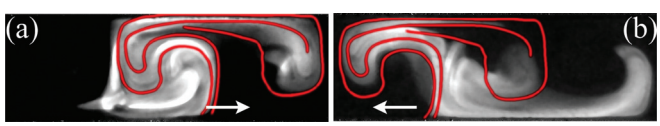

FIG. 8. Fronts triggered (a) to the left and (b) to the right of a pair of BIMs in a time-periodic vortex chain flow with the same experimental parameters as in Fig. 7. In each case, the front passes through the first BIM that it encounters and is then stopped by the second.

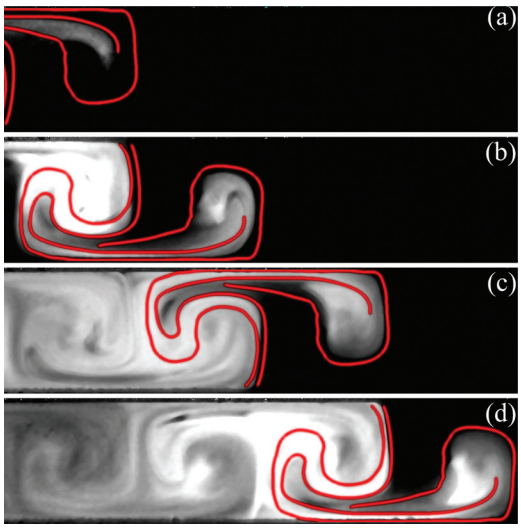

FIG. 9. Sequence of images of a front triggered at the left and propagating to the right in a time-periodic vortex chain flow; same experimental parameters as in Fig. 7. The images shown are taken in intervals of one period of oscillation. The red curves show the pair of BIMs immediately in front of the leading edge of the front. The front in this case mode-locks to the BIM structure.

The BIMs clearly play a significant role in the mode-locking behavior seen in previous experiments. Figure 9 shows four snapshots (taken at the same phase in successive periods of oscillation of the vortex chain) of the propagation of a front that is initially triggered off-screen to the left. The pair of BIMs directly in front of the leading edge of the reaction is shown in each image. The reaction front can be seen to converge onto the BIM within a couple of periods, and it remains locked to this BIM indefinitely after that, giving rise to the mode-locking behavior seen in earlier studies.

V. DISORDERED VORTEX ARRAY

Our studies of front propagation in the disordered vortex flow allow us to explore the applicability of the BIM formalism to more complicated and realistic flows. These experiments also (a) further demonstrate convergence of fronts on BIMs; (b) verify the oriented nature of the BIMs; and (c) verify that passive manifolds are the limiting case of burning manifolds for small v_0. Additionally, we explore the effect on front propagation of singularities from the projection of the 3D burning manifolds down to 2D (physical) space.

The velocity field measured for the disordered flow is shown in Fig. 10. The propagation of a BZ reaction front triggered near the top of the apparatus is shown in Fig. 11. The first three panels show raw images of the chemical front (with background subtraction). The pulse nature of the reaction is evident in the first image; most of the region behind the front has reset and is re-triggered in later images in the sequence as the reaction circulates back around the vortices. The last panel in Fig. 11 shows the results of image analysis to extract the leading edge of these three fronts. In this image, the reaction data shown in the first three panels are thresholded for intensity and smoothed, which removes much of the noise from the data. A Roberts-Cross edge

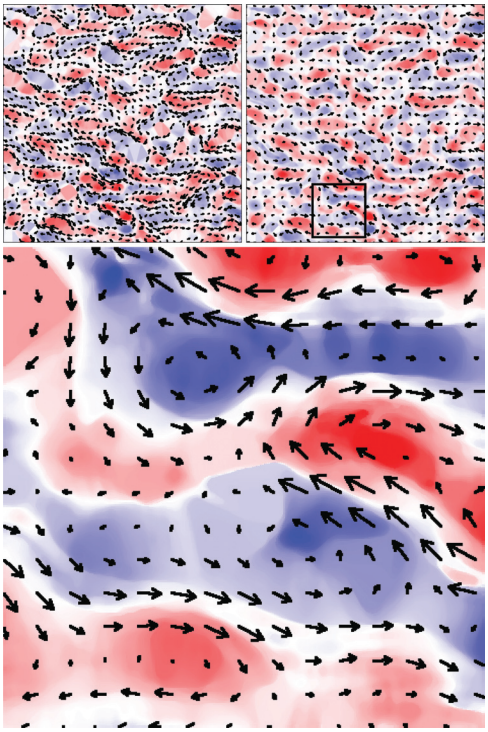

FIG. 10. Velocity field for the spatially disordered flow. (Top left) Irregular and sparse measured velocity data. (Top right) Velocity data interpolated to a uniform grid. Both panels show velocity field overlaid on a vorticity field (shown in red and blue) calculated from the interpolated velocity field. (Bottom) Enlarged velocity field, boxed region at bottom of top right image.

enhancement filter is then used to pick out the reaction front from the reaction bulk. To accentuate the visual clarity of the scheme, Fig. 11 has additionally had some noise manually removed and the reaction front has been thickened by dilating the pixels in the image. These additional image treatments were not applied to data used for analysis.

The time-independence of the disordered vortex flow allows us to utilize the gradient technique discussed in Sec. IV for Figure 7(g), here shown in Fig. 12. Wherever a BIM is present, the reaction front stops propagating (provided the front shares the orientation of the BIM), while in other regions, the front propagates freely. Therefore, by performing a superposition of gradient enhanced images, BIMs can be picked out as bright ridges in the image. In Figure 12, one particular reaction snapshot is shown in white, several gradient enhanced reaction fronts are shown in green, and the BIMs are shown in red. One can observe the green reaction fronts compounding along the BIMs as described.

The front shown in Fig. 12(a) is triggered experimentally at an Eulerian hyperbolic fixed point and converges onto nearby burning invariant manifolds, similar to the behavior seen with the time-independent vortex chain flow (Fig. 4). There is a pair of BIMs on either side of the trigger point that act as barriers, forming a channel through which the evolving front propagates.

The convergence and one-sided barrier nature of the BIMs can be seen with fronts triggered far away from the Eulerian fixed point, as seen in Figs. 12(b) and 12(c). These fronts still converge on the same BIMs as fronts triggered at

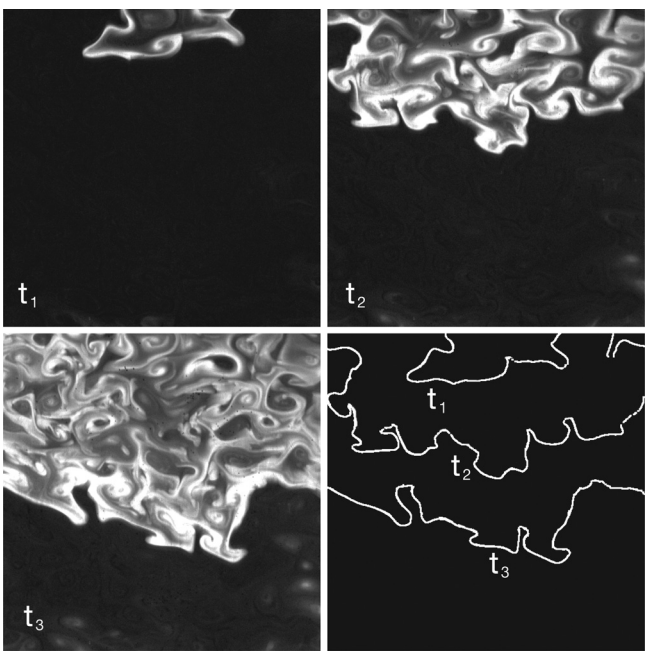

FIG. 11. Propagation of a BZ reaction front in the spatially disordered flow. The first three panels show the front at times t_1, t_2, and $t_3 = 240, 540$, and 840 s after the trigger. The fourth panel shows the extracted leading edges of these three fronts.

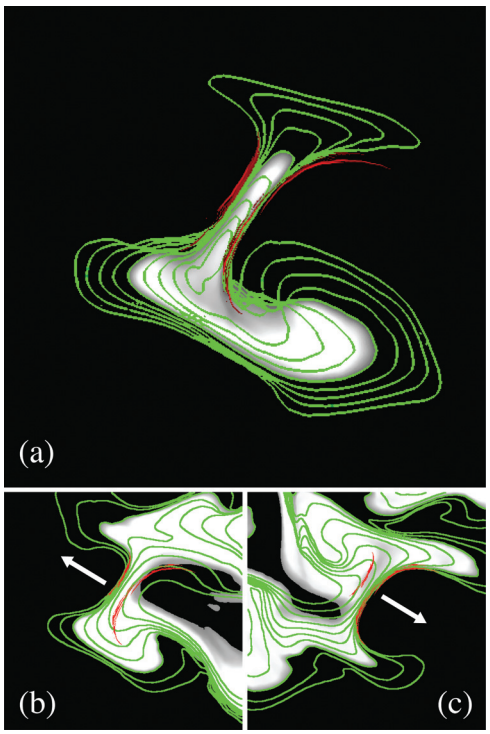

FIG. 12. Superposition of reaction fronts as they evolve in time. (a) Fronts extracted from a reaction triggered at a hyperbolic fixed point in the flow. An individual snapshot of the reaction is in white. Time-advanced reaction fronts appear in green. Experimentally extracted BIMs are in red. Each front shown is advanced in time by 10 s. (b) and (c) Propagation of fronts triggered away from the Eulerian fixed points. In these two images, the same BIM structures are shown (red). Arrows are added to indicate the direction of reaction propagation. Despite the fronts being triggered far away from the Eulerian fixed point, they still converge on the BIMs. Additionally one observes the left BIM blocking a left-propagating front and vice versa, while the other BIM is burned through (video online). [URL: http://dx.doi.org/10.1063/1.4746764.1]; [URL: http://dx.doi.org/10.1063/1.4746764.2].

the fixed point (Fig. 12(a)). The BIMs are attractors in phase space, and the strong convergence we observe in experiments for remote triggers agrees with this characterization. Additionally, Fig. 12 clearly shows that BIMs are oriented structures. In Fig. 12(b), one can see a front triggered to the right of the pair of BIMs propagating towards the left side of the frame. The front burns through the right BIM, which is oriented to the right, but the front stops cleanly on the left BIM, which shares the orientation of the front. Fig. 12(c) shows this same orientation phenomenon in the other direction.

We can also experimentally observe the dependence of the separation between BIMs upon the ratio $v_0 = V_0/U$ by varying the speed of the flow. In Fig. 13, we show three structures corresponding to three different ratios of v_0. One of these curves (the blue one) corresponds to the invariant manifold in the passive transport limit ($v_0 \to 0$), determined experimentally with the same magnetohydrodynamic techniques as used for the reaction, but replacing the reaction with a passive, neutrally buoyant dye. In this limiting case, the BIMs collapse onto one structure with no orientation—namely, the passive invariant manifold. As the non-dimensional burn speed v_0 increases, the separation between BIMs becomes greater.

Using our experimentally measured velocity field for the flow, we are able to theoretically predict the location of BIMs in the flow using the 3D ODE in Eq. (2). Theoretical calculations are performed by initializing a front element near a hyperbolic advective fixed point in the flow with an orientation angle θ whose normal is aligned with the stable direction of the advective fixed point. Equation (2) is then integrated using a 4th-order Runge-Kutte method. This calculation ideally results in the front element burning outward from the Eulerian fixed point toward the burning fixed point. Near the burning fixed point, the front element ideally makes a hard turn along one of the two unstable directions of the fixed point and proceeds to map out half of the BIM. This method allows for direct visualization of both the BIM and the splitting of the Eulerian fixed point into the two burning fixed points. Since one front element will burn toward a single burning fixed point and then turn down one of the two unstable directions, four front elements are needed to map out the BIM pair of each Eulerian fixed point.

These calculations are performed for the zoomed-in velocity field shown in the bottom panel of Fig. 10, corresponding to the experimentally determined BIMs from Figs. 12. These calculations match the upper branches of the experimentally extracted BIMs quite well, as shown in Fig. 14. The sparseness of the velocity data in this particular region leads to some discrepancies between the velocity field we used to calculate our BIMs and the actual flow field. For this reason, we are not able to calculate both unstable branches of the BIMs shown in Fig. 14. In regions of the flow with dense sampling of the velocity field, the simulations capture all branches of the BIMs.

Looking at a wider region of the spatially disordered flow, we experimentally measure BIMs throughout the entire apparatus (excluding a region near the sidewalls). Some of these experimentally measured BIMs are shown in Fig. 15(a). Using our measured velocity field, we can once again calculate BIMs in the flow. Theoretical calculations are performed for a sample of the BIMs in Fig. 15(a) and are shown overlaid on the experimental BIMs in Fig. 15(b).

These theoretical calculations of BIMs from the velocity field give further insight into front propagation dynamics. In the full 3D phase space of the system, the BIM is an infinitely long 1D curve. To visualize the BIM in the physical apparatus, we project this curve into the 2D xy-plane. When we perform this projection, the smooth BIM may appear to be kinked, due to the curve holding different values of θ at the same (x,y) coordinate. Some of these kinks can be observed in Fig. 15(b).

Fronts propagating along a BIM display interesting behavior when they encounter these kinks. The front will sometimes pinwheel around the kink, mirroring the behavior of the BIM in phase space (obtaining multiple values for the orientation at a single point in xy-space), as shown in

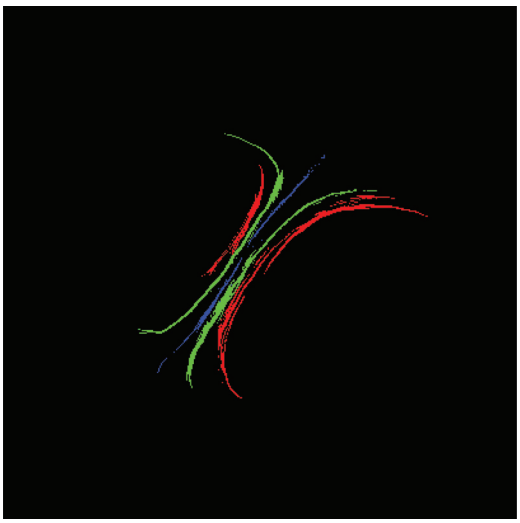

FIG. 13. BIMs measured with three values of the ratio $v_0 = V_0/U$; $v_0 = 0$, 0.11, and 0.18 for the blue, green, and red curves, respectively. The $v_0 = 0$ case is measured by detecting transport barriers for passive mixing.

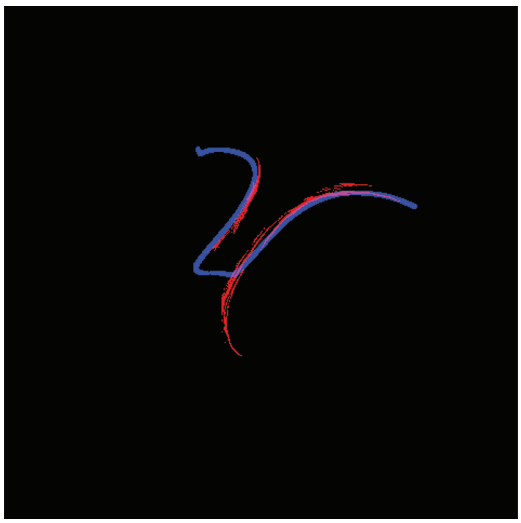

FIG. 14. Theoretical calculation (in blue) of the pair of BIMs, along with experimental BIMs (in red). While not all branches of these BIMs could be calculated, the branches shown are in good agreement with experiment.

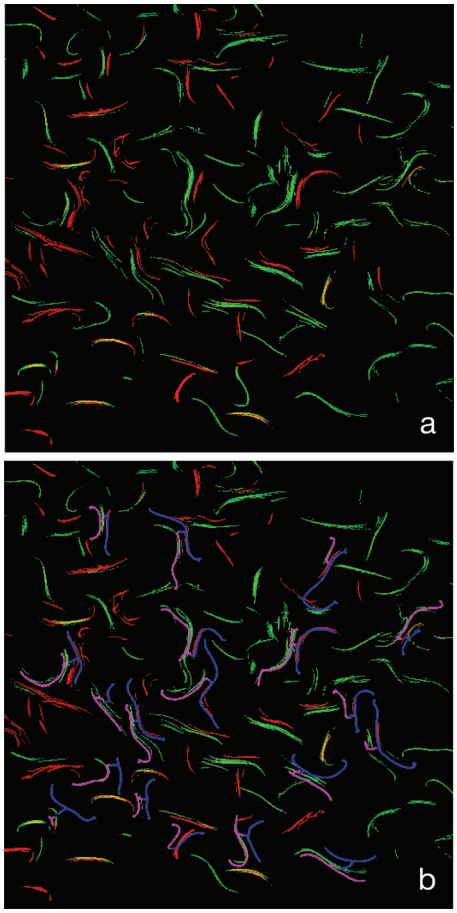

FIG. 15. A sample of experimentally measured BIMs for the disordered vortex array. (a) Green and red BIMs block fronts moving in opposite directions. Adjacent green and red BIMs are pairs arising from the splitting of the invariant manifold for passive mixing in that region. (b) Same experimental BIMs with theoretical calculations overlaid. Blue calculated BIMs match red experimental BIMs and magenta calculations match green (video online) [URL: http://dx.doi.org/10.1063/1.4746764.3].

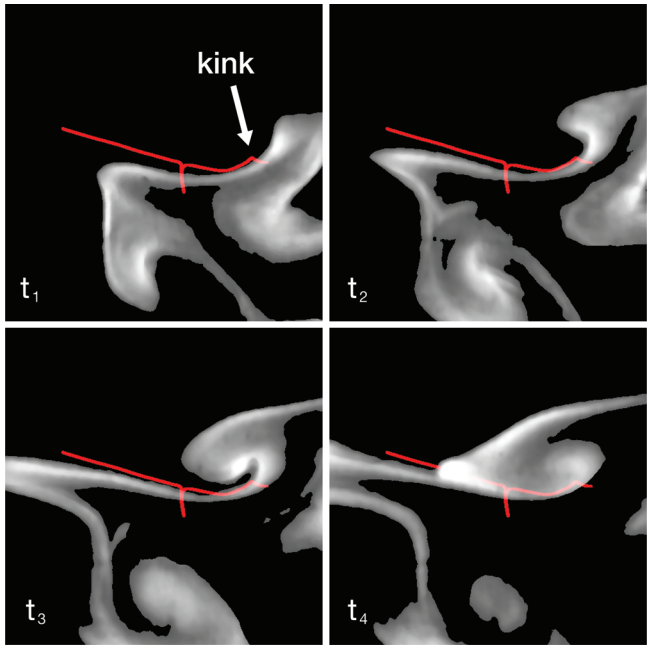

FIG. 16. These panels show a front pinwheeling around the projection kink of a theoretically calculated BIM (in red). Each panel is separated by 30 s (video online). [URL: http://dx.doi.org/10.1063/1.4746764.4]

Fig. 16. This mechanism enables the front to fill in the vortex cores around which BIMs tend to reside. It appears that the portion of the BIM which continues on after the kink has no clear physical significance in controlling front propagation,[49] though this issue must be explored further by experiment.

VI. DISCUSSION

In this paper, we present experimental results that establish the validity of a theory of BIMs (Ref. 11) as fundamental structures guiding the propagation of fronts in ARD systems. The BIMs act as one-way barriers for front propagation, blocking reactions propagating in one direction, but allowing reactions propagating in the opposite direction to pass. This framework works experimentally both for a vortex chain flow (both time independent and time periodic) and for a spatially disordered flow, indicating the likely generality of this approach.

Even though BIMs act as barriers to front propagation, they do not necessarily prevent long-range motion of the fronts nor do they necessarily prevent fronts from filling in regions within a flow. First, when projected down to 2D, the BIMs often form segments around which the fronts can wrap, as in Fig. 16. The same behavior occurs in the time-independent vortex chain flow; in Fig. 4, the red BIMs have similar cusps around which the fronts can pinwheel, thereby filling the vortex centers. Second, for time-periodic flows, the BIMs undulate periodically in time, and even though the fronts cannot pass through a similarly oriented BIM, they can follow the undulating BIMs across the system, as in the data for Figs. 6 and 7.

We are currently using the BIM formalism to analyze the previous experiments that showed front-pinning for vortex flows with an imposed wind.[37,38] It is our expectation that analysis will show that those time-independent flows contain BIMs that span the entire width of the system without 2D cusps; consequently, there is no possibility for fronts to wrap around the BIMs nor is there any time-dependence to enable long-range front propagation.

As shown in these experiments, BIMs can be successfully predicted, given the 3D ODEs (Eq. (2)) and a sufficiently resolved velocity field, even for spatially complicated flows. However, this formalism is rigorously valid only for time-independent and time-periodic flows. We are currently investigating the possibility of extending the formalism to time-aperiodic flows, using an approach similar to that used to extend the theory of passive invariant manifolds to Lagrangian coherent structures,[18] which act as temporary barriers to passive transport in more complicated flows.

Finally, it is our expectation that the BIM formalism will provide the basis for formulating a general theory to predict the speeds of reacting fronts in a range of advection-reaction-diffusion systems. Theory is already being developed[50] that uses the BIM formalism to explain the mode-locking that sets the propagation speeds often found for time-periodic flows. Furthermore, we are investigating an approach based on an extension of the theory of lobes[16,17]—regions formed from

the overlap of stable and unstable invariant manifolds—used to predict enhanced diffusivity due to chaotic mixing. Much in the way that lobes formed from invariant manifolds control long-range passive transport, it seems plausible that lobes can be defined from the overlap of BIMs and that this burning lobes can be used to predict front speeds.

ACKNOWLEDGMENTS

The authors would like to thank John Mahoney and Kevin Mitchell for their assistance in guiding both our theoretical and experimental inquiry in this work. These studies are supported by the U.S. National Science Foundation under Grants DMR-1004744 and PHY-0552790.

[1]D. Beule, A. Forster, and T. Fricke, Z. Phys. Chem. **204**, 1 (1998).
[2]A. Scotti and J. Pineda, J. Mar. Res. **65**, 117 (2007).
[3]C. A. Russell, D. L. Smith, L. A. Waller, J. E. Childs, and L. A. Real, Proc. R. Soc. London, Ser. B **271**, 21 (2004).
[4]*Handbook of Crystal Growth*, edited by D. T. J. Hurle (North-Holland, Amsterdam, 1993), Vol. 1B.
[5]T. Tel, A. de Moura, C. Grebogi, and G. Karolyi, Phys. Rep. **413**, 91 (2005).
[6]S. K. Scott, *Oscillations, Waves, and Chaos in Chemical Kinetics* (Oxford University Press, Oxford, 1994).
[7]T. John and I. Mezic, Phys. Fluids **19**, 123602 (2007).
[8]I. Prigogine and I. Stengers, *Order Out of Chaos: Man's New Dialogue with Nature* (Bantam, New York, 1984).
[9]A. Babloyantz, *Molecular Dynamics and Life: An Introduction to Self-Organization of Matter* (Wiley, New York, 1986).
[10]M. Sandulescu, C. Lopez, E. Hernandez-Garcia, and U. Feudel, Ecol. Complexity **5**, 228 (2008).
[11]J. Mahoney, D. Bargteil, M. Kingsbury, K. Mitchell, and T. Solomon, Europhys. Lett. **98**, 44005 (2012).
[12]H. Aref, J. Fluid Mech. **143**, 1 (1984).
[13]R. S. MacKay, J. D. Meiss, and I. C. Percival, Physica D **13**, 55 (1984).
[14]J. M. Ottino, *The Kinematics of Mixing: Stretching, Chaos and Transport* (Cambridge University Press, Cambridge, 1989).
[15]S. Wiggins, *Chaotic Transport in Dynamical Systems* (Springer-Verlag, New York, 1992).
[16]R. Camassa and S. Wiggins, Phys. Rev. A **43**, 774 (1991).
[17]T. H. Solomon, S. Tomas, and J. L. Warner, Phys. Rev. Lett. **77**, 2682 (1996).
[18]G. A. Voth, G. Haller, and J. P. Gollub, Phys. Rev. Lett. **88**, 254501 (2002).
[19]C. Coulliette, F. Lekien, J. D. Paduan, G. Haller, and J. E. Marsden, Environ. Sci. Technol. **41**, 6562 (2007).
[20]F. Lekien, C. Coulliette, A. J. Mariano, E. H. Ryan, L. K. Shay, G. Haller, and J. Marsden, Physica D **210**, 1 (2005).
[21]I. Mezic, S. Loire, V. A. Fonoberov, and P. Hogan, Science **330**, 486 (2010).
[22]A. C. Haza, T. M. Ozgokmen, A. Griffa, Z. D. Garraffo, and L. Piterbarg, Ocean Modell. **42**, 31 (2012).
[23]R. J. Field and M. Burger, *Oscillations and Traveling Waves in Chemical Systems* (Wiley, New York, 1985).
[24]B. Shraiman, Phys. Rev. A **36**, 1374 (1987).
[25]T. Solomon and J. Gollub, Phys. Fluids **31**, 1372 (1988).
[26]T. H. Solomon and J. P. Gollub, Phys. Rev. A **38**, 6280 (1988).
[27]T. H. Solomon, A. T. Lee, and M. A. Fogleman, Physica D **157**, 40 (2001).
[28]M. Abel, A. Celani, D. Vergni, and A. Vulpiani, Phys. Rev. E **64**, 046307 (2001).
[29]M. Abel, M. Cencini, D. Vergni, and A. Vulpiani, Chaos **12**, 481 (2002).
[30]M. Cencini, A. Torcini, D. Vergni, and A. Vulpiani, Phys. Fluids **15**, 679 (2003).
[31]M. S. Paoletti and T. H. Solomon, Europhys. Lett. **69**, 819 (2005).
[32]M. S. Paoletti and T. H. Solomon, Phys. Rev. E **72**, 046204 (2005).
[33]T. H. Solomon and I. Mezić, Nature **425**, 376 (2003).
[34]To get a more precise representation of the manifold, we integrate for one period, after which the tracers map out a segment of the manifold. The coordinates of the tracers in this segment are then integrated through another period, and the new locations are combined with those from the original segment. These new coordinates are integrated through another period, and these new locations are combined with those from previous segments. This process is repeated through several periods of oscillation.
[35]R. A. Fisher, Ann. Eugen. **7**, 355 (1937).
[36]A. N. Kolmogorov, I. G. Petrovskii, and N. S. Piskunov, Moscow Univ. Math. Bull. **1**, 1 (1937).
[37]M. Schwartz and T. H. Solomon, Phys. Rev. Lett. **100**, 028302 (2008).
[38]G. M. O'Malley, M. S. Paoletti, M. E. Schwartz, and T. H. Solomon, Commun. Nonlinear Sci. Numer. Simul. **16**, 4558 (2011).
[39]C. Torney and Z. Neufeld, Phys. Rev. Lett. **99**, 078101 (2007).
[40]N. Khurana, J. Blawzdziewicz, and N. T. Ouellette, Phys. Rev. Lett. **106**, 198104 (2011).
[41]J. R. Boehmer and T. H. Solomon, Europhys. Lett. **83**, 58002 (2008).
[42]H. Willaime, O. Cardoso, and P. Tabeling, Phys. Rev. E **48**, 288 (1993).
[43]K. Matthiessen, H. Wilke, and S. C. Muller, Phys. Rev. E **53**, 6056 (1996).
[44]D. A. Vasquez and E. Thoreson, Chaos **12**, 49 (2002).
[45]H. Kitahata, R. Aihara, N. Magome, and K. Yoshikawa, J. Chem. Phys. **116**, 5666 (2002).
[46]L. Rongy and A. D. Wit, J. Chem. Phys. **124**, 164705 (2006).
[47]L. Rongy and A. D. Wit, J. Chem. Phys. **131**, 184701 (2009).
[48]We also use the symmetry of the flow to include flipped versions of the front at odd multiples of π as well.
[49]J. Mahoney and K. Mitchell, Chaos **22**, 037104 (2012).
[50]J. Mahoney and K. Mitchell, private communication (2012).